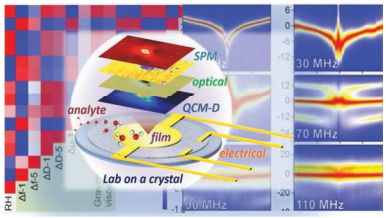

Schematic representation of lab-on-a-crystal where macroscale optical, gravimetric, viscoelastic and electrical measurements can be correlated with spatially resolved Raman, photoluminescence measurements on micron scale, and nanoscale scanning probe mechanical properties on the same film.

ADVANCED FUNCTIONAL MATERIALS
www.afm-journal.de

Machine Learning-Enabled Correlation and Modeling of Multimodal Response of Thin Film to Environment on Macro and Nanoscale Using "Lab-on-a-Crystal"

*Eric S. Muckley, Liam Collins, Bernadeta R. Srijanto, and Ilia N. Ivanov**

To close the feedback loop between artificial intellegence-controlled materials synthesis and characterization, material functionality must be rapidly tested. A platform for high-throughput multifunctional materials characterization is developed using a quartz crystal microbalance with auxiliary in-plane electrodes and a custom gas/vapor flow cell, enabling simultaneous scanning probe microscopy and electrical, optical, gravimetric, and viscoelastic characterization on the same film under controlled environment. The lab-on-a-crystal in situ multifunctional output allows direct correlations between the gravimetric/viscoelastic, electrical, and optical responses of polymer film in response to environment. When multiple film properties are used to augment the training set for machine learning regression, prediction of material response to environment improves by a factor of 13 when <5% of the total dataset is used for model training.

1. Introduction

High-throughput systems for assessing thin film response (optical, electrical, viscoelastic, gravimetric) to environment are important for development of the understanding of material structure–function relationships, accelerating advanced material discovery, and development of novel applications.[1] Currently multimodal testing requires specialized instrument design.[2] The last 35 years of research and development of microfabrication, miniaturization of chemical reactors, mixing, and separation techniques as well design of miniaturized analytical instruments (optical, electrical, electrochemical, mass-spectrometric, nuclear magnetic resonance spectroscopy) has led to design of microfluidic lab-on-a-chip systems in which multiple functionalities of a single liquid sample are probed simultaneously.[3] While over 600 micro total analysis systems for multimode characterization of liquid samples were reported, we are yet to see an analog for multimodal characterization of thin films. Characterization of the structure–function relationship of thin films often requires transparent or dielectric substrates for optoelectronic measurements and a separate elastomer substrate (such as polydimethylsiloxane) for mechanical measurements, making it challenging for simultaneous multimodal experiments.[4] Mechanical testing of flexible electronics is often carried out on hermetically sealed devices that prohibits probing of environmental effects[5] or on highly integrated flexible chips that are not suitable for high-throughput screening.[6] Rapid screening of thin film properties commonly focuses on optimization of a specific functionality[2b,7] rather than testing of multiple functions simultaneously. Growing interest in multifunctional films across a broad range of potential applications indicates the need for development of a single substrate that can accommodate mechanical/structural, electrical, optical, and local microscale measurements.[8]

In this study, we investigated a quartz crystal microbalance (QCM) as the foundation for a multifunctional materials characterization platform, enabling simultaneous macro-scale electrical, optical, gravimetric/viscoelastic measurements, and nanoscale characterization of the same film under controlled environment. The QCM is a thickness-shear mode piezoelectric resonator used for probing gravimetric[9] and viscoelastic properties[10] of thin films in vacuum, gas, and liquid environments. Its sub-nanogram mass sensitivity has made the QCM an integral tool for thin film processing, environmental monitoring, machine olfaction, and biomedical sensing.[11] When used in conjunction with additional characterization techniques, QCM enables measurements of gravimetric/viscoelastic film response during gas/vapor sorption, providing valuable insight into effects of environment on the behavior of functional thin films.[12]

Multifunctional film characterization on a QCM surface is generally not possible using commercially available systems because of lack of flexibility in crystal mounting hardware, flow cell geometry, and other technical issues. To enable in-plane electrical characterization of thin films, we deposited auxiliary electrodes on the QCM surface. A custom 3D printed gas/vapor flow cell was used to maintain controlled environment around the crystal, with a quartz window for optical access to the film. We investigated viscoelastic response of hydroscopic polymer film poly(3,4-ethylenedioxythiophene)-poly(styrenesulfonate) (PEDOT:PSS) under changing relative humidity (RH) while probing simultaneous electrical, optical, and nanoscale

E. S. Muckley, L. Collins, B. R. Srijanto, I. N. Ivanov
Center for Nanophase Materials Sciences
Oak Ridge National Laboratory
P.O. Box 2008, Oak Ridge, TN 37831, USA
E-mail: ivanovin@ornl.gov
The ORCID identification number(s) for the author(s) of this article can be found under https://doi.org/10.1002/adfm.201908010.

DOI: 10.1002/adfm.201908010

morphological changes in the film using multi-frequency QCM with energy dissipation monitoring (QCM-D). PEDOT:PSS was used as a test sample because of its importance in organic optoelectronic devices and its reversible gravimetric/viscoelastic,[13] optical, and electrical response to water vapor.[12b,14] The results demonstrate viability of the lab-on-a-crystal platform for simultaneous measurements of electrical, optical, and gravimetric/viscoelastic properties of thin film under controlled environment on macro and nanoscales.

2. Experimental Section

Polished 10 MHz QCM crystals with pre-patterned gold electrodes were purchased from OpenQCM (www.openqcm.com). Auxiliary gold electrodes were deposited on edges of the QCM (see **Figure 1**) using dual gun electron beam evaporation method followed by dry lift-off. PEDOT nanoparticle dispersion in H_2O with dodecylbenzene sulfonic acid dopant was purchased from Sigma Aldrich. Poly(4-styrene sulfonic acid) (PSS) solution (18% by weight in H_2O) was purchased from Sigma Aldrich. The PEDOT dispersion was mixed with PSS solution in a 1:2 ratio and sonicated for 30 min to promote mixing. A 6 µL solution of the PEDOT:PSS mixture was drop-cast on the QCM crystal. After drying in air for 20 min, the resulting PEDOT:PSS thin film covered the central QCM electrode and spanned the width of the auxiliary electrodes, allowing in-plane electrical measurements.

A schematic diagram of the experimental configuration is shown in Figure 1a. Electrical leads were attached to the auxiliary gold electrodes using silver paste (Ted Pella, Inc.). For water adsorption experiments, a custom gas/vapor flow cell was designed and printed using a Snapmaker 3D printer. The crystal was mounted inside the flow cell using two standard spring-loaded clips. Two ports at opposite corners of the flow cell served as an inlet and outlet for gas/vapor. A circular aperture in the flow cell ceiling (see Supporting Information) was designed to accommodate an optical microscope objective and served as a window for optical measurements. Humidity was controlled using an L&C Science and Technology RH-200 RH generator with dry nitrogen as a carrier gas. The humidity generator was controlled using custom software written in LabVIEW. An N_2/H_2O vapor mixture was injected into the a flow cell step-wise to produce RH levels from 2% to 95%. Impedance of the QCM crystal was measured using a SARK-110 antenna analyzer. Analysis and modeling of QCM impedance spectra were performed using custom software written in Python. Photoluminescence (PL) and Raman spectroscopy were done with a Renishaw Qontour inVia Raman microscope in backscattering geometry through a 50 × (NA = 0.95) objective, using a 532 nm laser for excitation. Optical transmittance was measured using a halogen lamp as white light source and USB2000 Ocean Optics UV–vis spectrometer. A Zahner IM6 electrochemical workstation was used for AC electrical measurements, and a Keithley 2420 with custom LabVIEW software was used for DC electrical characterization of the film. All scanning probe

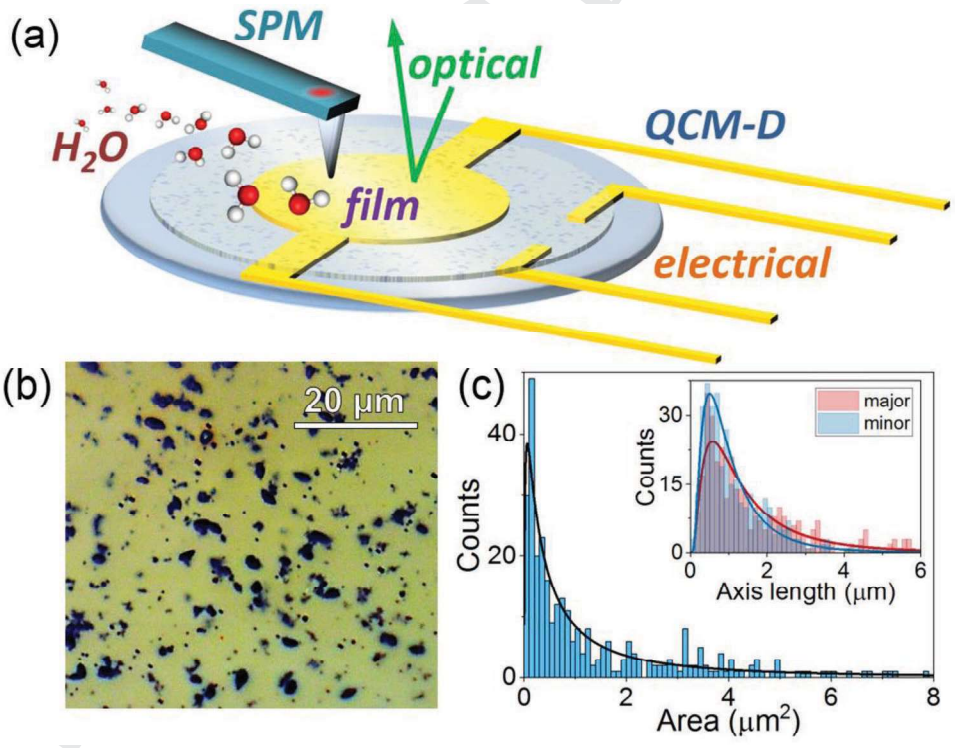

Figure 1. a) Schematic diagram of experimental configuration. A QCM crystal with auxiliary electrodes was coated with PEDOT:PSS film and used as a platform for macroscale electrical, optical, and gravimetric (QCM-D) probing along with local characterization by scanning probe microscopy (SPM). b) Optical microscope image of PEDOT:PSS film on central gold QCM electrode containing dark-colored PEDOT aggregates inside PSS matrix. c) Histogram of average PEDOT aggregate area, with average lengths of major and minor ellipsoid axes shown in inset. Fit lines show lognormal distributions.

microscopy (SPM experiments were performed using a commercial Cypher-ES atomic force microscope (AFM) equipped with a BlueDrive photothermal excitation (Asylum Research–an Oxford Instruments Company, Santa Barbara, CA). The cantilever used for imaging was an AC160 (Olympus, Tokyo, Japan) with a calibrated spring constant ($k \approx 30.427$ N m^{-1}) and resonance frequency ≈277 kHz. A bimodal AFM technique using a hybrid amplitude/frequency-modulated detection scheme AMFM was used for nanomechanical mapping. Principles of the AM-FM mode are described elsewhere.[15] For nanomechanical mapping under changing RH levels, the inlet for the environmental scanner was supplied with a continuous flow of N_2, diverted from a homemade gas humidifier. Humidity was measured near the microscope cell by an auxiliary humidity probe. At each humidity level, the cell environment was stabilized for ≈30 min before commencement of the adhesion measurement. All measurements were performed at room temperature and atmospheric pressure.

3. Results and Discussion

3.1. Optical and SPM Characterization of PEDOT:PSS Film

Optical microscope images of PEDOT:PSS film deposited on the gold-coated QCM crystal revealed PEDOT aggregates with average area between ≈500 nm^2 and ≈10 μm^2. Aggregates were distributed uniformly across the film surface (Figure 1b). The histogram of aggregate area followed a lognormal distribution with average area ≈1.2 μm^2 (Figure 1c). Aggregates were ellipsoidal with average major axis length ≈50% larger than average minor axis length (Figure 1c inset). Histograms of individual axis lengths followed lognormal distributions. While many studies report properties of commercial PEDOT:PSS dispersion (Baytron P-V4, HC Starck) containing PEDOT domains of 50 nm dimeter or less,[16] we used undispersed PEDOT nanoparticles with the goal of providing high contrast in optical and scanning probe measurements. The resulting PEDOT:PSS film contained well-defined PEDOT domains and exhibited a significantly different electrical response to RH than our previously studied PEDOT:PSS films deposited from commercial dispersions.[12b] The effect of morphology on electrical properties of PEDOT:PSS films was studied elsewhere.[17]

SPM was used to correlate local morphology and elastic modulus with film properties obtained on the macroscale. We note that quantification of nanomechanical measurements on heterogenous samples is challenging due to unknown geometry of the probe, elastic constant of the cantilever, and validity of the contact mechanical model that describes the indentation process. Additional complications arise due to interactions with the underlying substrate or polymer matrix. Here, we focus on qualitative correlations between macroscale and local SPM measurements in order to highlight the advantages of multiscale probing of heterogeneous films. **Figure 2** shows mapping of a PEDOT aggregate using a) optical microscopy; b) PL, c) SPM topography; and d) elastic modulus derived from SPM measurements. Additional SPM results are shown in the Supporting Information. The PEDOT aggregate consists of an ellipsoidal domain ≈3 μm long with a smaller rounded domain near its lower right-hand corner. PL is localized near the center of the domains and is highest at the center of the larger aggregate. The large PEDOT aggregate protrudes from the surrounding PSS matrix. Mapping of elastic modulus reveals that the PEDOT aggregate is softer than the surrounding PSS matrix by ≈3 GPa, which is consistent with previous reports.[18]

To correlate SPM measurements with macroscale optical measurements, the height profile, elastic modulus, and PL intensity were extracted from Figure 2b–d and compared along two different cross-sectional profiles (shown in Figure 2a). In profile 1 (Figure 2e), changes in PL, height, and elastic modulus are strongly correlated across the PEDOT aggregate, indicating consistency between different functional mapping modes. Profile 2 shows that the presence of smaller dispersed PEDOT aggregates to the right-hand side of the large aggregate is detected by changes in modulus but the aggregate was not detected in optical maps, which highlights the importance of using complementary mapping modes.

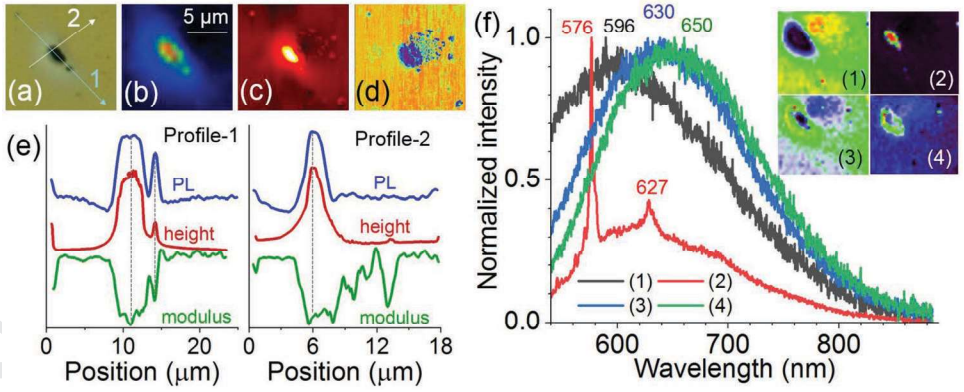

Figure 2. PEDOT aggregate in PSS matrix imaged by a) optical microscopy, b) photoluminescence (PL), c) SPM topography, and d) SPM-derived elastic modulus. In panel (b), PL is normalized (black color corresponds to 0 and red color corresponds to 1). In panel (c), black color corresponds to 0 nm and white color corresponds to 500 nm. In panel (d), yellow color corresponds to 3 GPa and purple color corresponds to 0 GPa. e) Qualitative comparison of PL, topography (height), and elastic modulus across the two profiles shown in panel (a). Vertical dashed lines correspond to the center of the large PEDOT aggregate. The PL map in panel (b) was deconvoluted into four principal components, represented by the four spectra in panel (f). The contribution of each component is shown in the inset of panel (f).

We investigated PL response of the film by deconvoluting the PL map in Figure 2b into four principal components (PCs) that explain 98% of the variance in PL response. The four PCs correspond to PL emission centered at 596, 630, and 650 nm, and peaks at 576 and 627 nm assigned to Raman scattering (Figure 2f). The contribution of each PC to the total PL map is shown in the inset of Figure 2f. PC-1 loading is highest at the small PEDOT aggregates to the right of the large aggregate. The Raman signatures associated with PC-2 suggest that it is related to semi-crystalline PEDOT in the center of the aggregate. Contributions from the PSS spectral features are visible in PC-3 and PC-1, while contributions from the interfaces between PSS and the large PEDOT aggregate are visible in PC-4.

The effect of humidity on optical transmittance of the film was measured by passing light from a halogen lamp through the PEDOT:PSS-coated QCM crystal and collecting transmitted light at a lens on the opposite side of the flow cell using an optical fiber and UV–vis spectrometer. As RH increased, absorption of the transmitted light decreased, and the wavelength of maximum intensity increased (see Supporting Information). Changes in the intensity of transmitted light likely occurred as a result of swelling of PSS, which increased the optical path length through the film and led to higher attenuation of the beam.

3.2. Gravimetric/Viscoelastic Response to Humidity

The 10 MHz resonant frequency QCM crystal used as a substrate for PEDOT:PSS film enabled gravimetric and viscoelastic probing of the film under changing RH conditions. A mixture of dry N_2 and H_2O vapor was injected into the QCM flow cell to produce RH levels from 2% to 95% in 5% steps (bottom panel in **Figure 3**a). QCM-D measurements were carried out at the fundamental, third, fifth, seventh, ninth, and eleventh crystal harmonics. Normalized frequency shifts ($\Delta f/n$, where n is the crystal harmonic number) and changes in dissipation ($\Delta D/n$) exhibited roughly symmetric response during increasing and decreasing RH levels, demonstrating reversible response of the film to water (Figure 3a). Changes in $\Delta f/n$ and $\Delta D/n$ occurred primarily at the first three odd crystal harmonics while ninth and eleventh overtones showed insignificant response to RH.

Full QCM conductance spectra are shown in Figure 3b. Spectra were normalized for direct comparison of response at different crystal harmonics (blue = 0, red = 1). The fundamental harmonic (10 MHz) exhibited Sauerbrey-like response,[9a] decreasing with RH as adsorption of water led to an increase in film mass. Conductance spectra at seventh, ninth, and eleventh harmonics contained signatures of inharmonic spurious overtone resonances ≈10–20 kHz above and below the main resonant peaks that are common in high-frequency resonators.[19] Frequency shifts at the third, fifth, and seventh harmonics (corresponding to 30, 50, and 70 MHz resonances) decreased with RH at low humidity and exhibited sharp reversible increases at RH > 85%. Voinova et al. attributed this anomalous "missing mass effect"[9b] to viscous loss in the film, which is consistent with our previous study that showed nonmonotonic change in viscosity of PEDOT:PSS with increasing RH.[14a] Several previous studies have attributed the missing mass effect to slip or decoupling at the film–crystal interface.[20] To investigate the effect further, we note that harmonic dependence of Δf and ΔD suggests that changes in viscoelastic behavior did not occur uniformly throughout the film. The penetration depth (δ) at which amplitude of the acoustic shear wave decreases to $1/e$ of its value at the crystal surface is $\delta = (\eta/2\pi f\rho)^{1/2}$, where η, f, and ρ are viscosity, resonant frequency, and density of the adsorbent film, respectively.[21] We used a continuum mechanics model[10a] to estimate shear modulus (μ) and viscosity (η) of the PEDOT:PSS

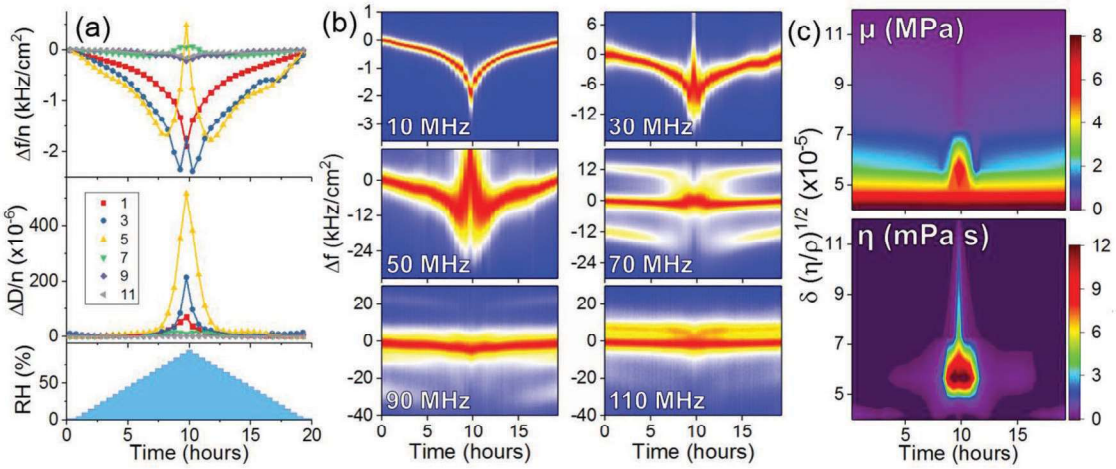

Figure 3. a) Frequency shift ($\Delta f/n$, top panel) and dissipation ($\Delta D/n$, middle panel) normalized to crystal harmonic number (n) during exposure to relative humidity (RH) increasing and decreasing step-wise from 2% to 95% as shown in bottom panel. Numbers in legend correspond to crystal harmonic number. Plotted points are experimental data, lines show fits to Voinova model.[10a] b) Full normalized conductance spectra of QCM crystal during exposure to changing RH. Color bar shows normalized conductance (blue = 0, red = 1), vertical axes show frequency shifts (Δf) of resonant peaks, and horizontal axes show time. Each panel in (b) corresponds to a different crystal harmonic, from the fundamental harmonic (10 MHz) to the 11th harmonic (110 MHz). c) Shear modulus (μ) and viscosity (η) of film as a function of time and penetration depth (δ) of the QCM shear wave. The value of δ is expressed in terms of film density (ρ) and viscosity (η). In panels (b) and (c), the sequence of RH over time is the same as that shown in the bottom panel of (a).

film as a function of penetration depth during sorption/desorption of water vapor (Figure 3c). Due to the complexity of changing density and viscosity of the film as it adsorbed water, penetration depth was reported in units of $(\eta/\rho)^{1/2}$, where $\delta = 0$ corresponds to the film-crystal interface. Using constant values of $\rho = 1.1$ g cm^{-3}[22] and $\eta = 9 \times 10^{-4}$ Pa s,[23] we estimated that the film depth in Figure 3c was probed from ≈34 to ≈114 nm from the film-crystal interface. As expected, μ was highest at the film-crystal interface due to strong film-crystal coupling and poor diffusion of water through the film. Changes in μ and η at $\delta < 5$ were negligible, which suggest that film-crystal coupling at the interface was not disrupted even at high RH. The largest viscoelastic response to water occurred in the center of the film ($\delta \approx 6$) due to viscous loss in the PSS matrix. Water adsorption led to disruption of hydrogen bonding between PSS, which decreased mechanical coupling between the water-saturated film surface ($\delta > 7$) and the more rigidly coupled film-crystal interfacial region ($\delta < 5$). The interface between high-shear modulus and low-shear modulus regions exhibited the largest viscoelastic change with humidity, which is consistent with mechanisms proposed by others in which adsorption leads to formation water meniscus layers that disrupt hydrogen bonding and facilitate solvation of ambient gas.[24] The results are consistent with elastic moduli of PEDOT and PSS in dry and wet states reported by others,[18] including Lang et al. who showed that PEDOT:PSS elastic modulus decreased from 2.8 to 0.9 GPa when RH increased from 23% to 55%.[13]

3.3. Electrical Response to Humidity

DC electrical characterization of PEDOT:PSS film was carried out using auxiliary electrodes deposited on the QCM surface. Electrical response was measured in-plane with 5 mm spacing between electrodes. Current–voltage (IV) characteristics were measured across PEDOT:PSS film on the QCM surface from –2V to +2V bias with 20 mV s^{-1} sweep rate. The film exhibited roughly 4 orders of magnitude increase in current from 2% to 95% RH (**Figure 4**a) and showed roughly linear IV characteristics with <5% hysteresis when voltage sweep direction was reversed. The linear IV characteristics are in agreement with those reported in other studies of PEDOT:PSS films.[24,25]

Figure 4b shows reversibility of the IV characteristics as RH was cycled from 2% to 95% and back to 2% (RH is shown in blue on the far time axis). To investigate reversibility, the current measured at +2V was extracted from IV curves during wetting and drying processes. The current showed reversibility to within 50 pA after the film was returned to 2% RH conditions (Figure 4c).

Recently, it was shown that films with PEDOT to PSS ratio of 1:0.6 increases conductivity during swelling while film with 1:4 ratio decreases conductivity during swelling.[26] This mechanism was attributed to aggregation of PEDOT cores that increases average conductive pathway length in PEDOT-rich PSS matrix, and increased distance between adjacent PEDOT cores in PSS-rich film. This is consistent with the present findings in 1:2 ratio PEDOT:PSS film.

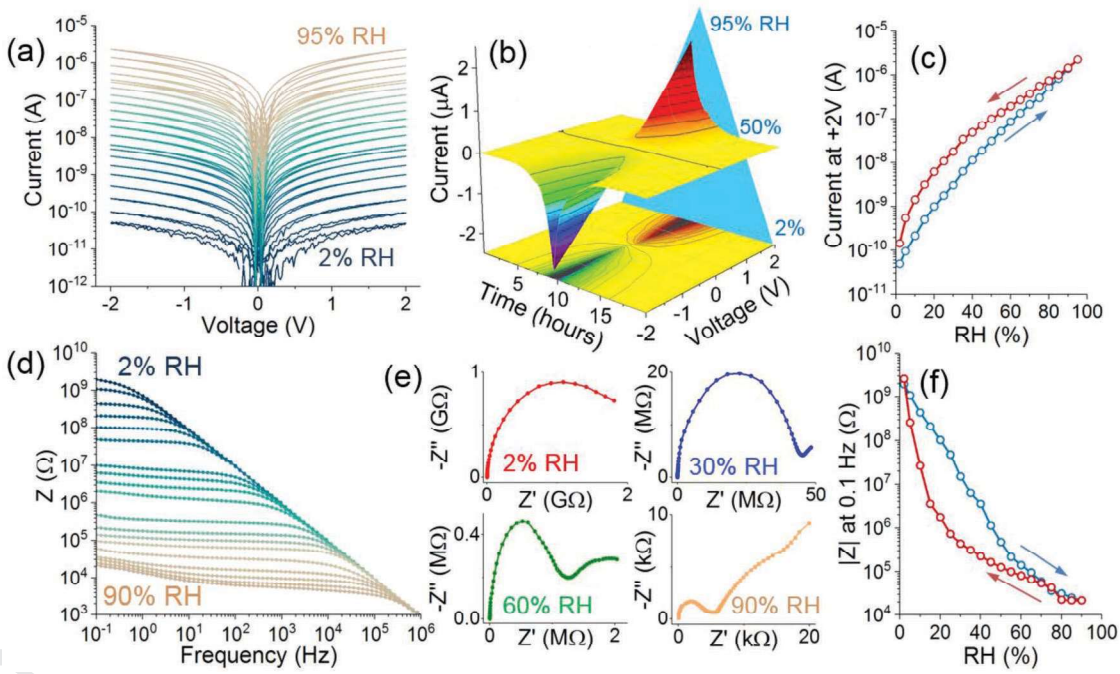

Figure 4. a) Log-scale IV characteristics of PEDOT:PSS film measured on surface of QCM from 2% to 95% RH. b) Linear-scale IV characteristics measured over time showing reversibility of current change with RH. Schematic of RH ramp is shown in blue spanning the time axis. c) Current measured across PEDOT:PSS film under +2 V bias under increasing (blue curve) and decreasing (red curve) RH. d) Frequency-dependent electrical impedance (Z) of PEDOT:PSS film measured from 2% to 90% RH. e) Nyquist representation of electrical impedance (imaginary impedance Z'' vs real impedance Z') measured at 2% (red), 30% (blue), 60% (green), and 90% (yellow) RH. f) Magnitude of low-frequency electrical impedance ($|Z|$) measured at 0.1 Hz under increasing (blue) and decreasing (red) RH.

Others also found PEDOT:PSS ratio-dependent changes in electrical resistance and argue that initial film morphology is primary factor that controls how conductivity changes during film strain.[27]

It is worth noting that some studies reported conductivity decrease in commercial PEDOT:PSS dispersions during uptake of water. This was attributed to swelling of the PSS matrix that increased the distance between adjacent conductive PEDOT domains.[12b,28] Since PEDOT aggregates in the current study are large and highly localized, electrical conductivity is dominated by charge transport that occurs through the PSS matrix. It was shown previously that water adsorption on PSS result in formation of hydronium and charged sulfonic groups (H_2O + $PSS(HSO_3) \rightarrow H_2O^+ + PSS(SO_3)^+$),[14a,24] leading to formation of mobile ionic species that may contribute to charge transport. Evidence of ionic diffusion at low frequencies was observed at high RH in Nyquist plots in Figure 4e.

Electrical impedance of the PEDOT:PSS film was measured from 1 to 8 MHz with 50 mVAC excitation and 0 VDC offset. Bode plot of total impedance (Z) is shown in Figure 4d. Impedance of the film measured at 0.1 Hz decreased from ≈2 GΩ to 20 kΩ as RH increased from 2% to 90%. Changes in impedance were most significant at low frequencies, while impedance measured at 1 MHz remained constant at ≈1 kΩ across the measured humidity range. Nyquist plots of the impedance at different RH levels show a complex transition from one primary semicircle at 2% RH to two semicircles at 60% RH and three semicircles at 90% RH (Figure 4e). Appearance of additional semicircles in the Nyquist plots suggests that additional conduction channels are activated as water loading of the film increases. Formation of a water meniscus on the film surface may provide a network for charge conduction at RH ≈30%,[24] while hydronium formation may enhance ionic mobility inside the film at RH ≈90%,[14a,24] leading to further decrease in impedance. To quantify reversibility of the low-frequency impedance after removal of water from the film, impedance measured at 0.1 Hz was plotted during increasing and decreasing RH (Figure 4f). Impedance showed reversibility to within 90% of its initial value before exposure to humidity and exhibited the largest hysteresis in impedance at low RH, in agreement with current hysteresis shown in Figure 4c.

Table 1. Measured properties of PEDOT:PSS film used for training predictive regression model.

Symbol	Description and units	Functional mode
$\Delta\lambda$	Wavelength of maximum absorption change [nm]	Optical
ΔI	Maximum intensity change [counts]	Optical
IDC	DC current at +2VDC bias [μA]	Electrical
Phase	AC phase at 10 Hz [rad]	Electrical
Z-10 Hz	AC impedance at 1 Hz [MΩ]	Electrical
Z-0.1 Hz	AC impedance at 0.1 Hz [MΩ]	Electrical
$\Delta\eta$-n	Viscosity change at nth QCM harmonic [Pa s]	Gravimetric/viscoelastic
$\Delta\mu$-n	Shear modulus change at nth QCM harmonic [Pa]	Gravimetric/viscoelastic
ΔD-n	Dissipation change at nth QCM harmonic [$\times 10^{-6}$]	Gravimetric/viscoelastic
Δf-n	Frequency shift at nth QCM harmonic [kHz cm^{-2}]	Gravimetric/viscoelastic
RH	Relative humidity [%]	Environmental

3.4. Multimode Prediction Using Machine Learning Regression

To explore the benefits of characterizing multiple film functionalities on a single substrate, we investigated correlations between the gravimetric/viscoelastic, electrical, and optical humidity responses of PEDOT:PSS film. The bivariate (Pearson) correlation coefficient was used to quantify linear association between 14 film parameters as they varied with RH. Descriptions of each parameter are displayed in **Table 1**. The bivariate coefficients are shown in **Figure 5**a separated by functional mode

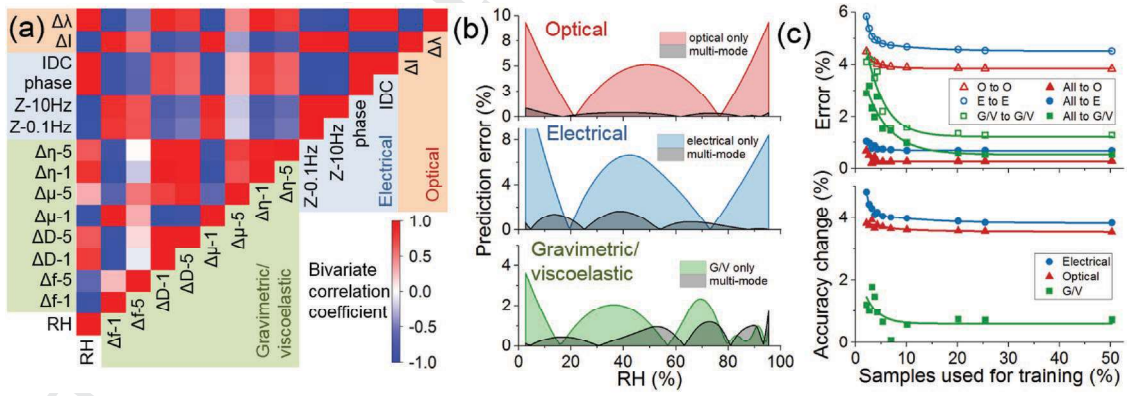

Figure 5. a) Bivariate (Pearson) correlations between measured gravimetric/viscoelastic (green), electrical (blue), and optical (red) properties of PEDOT:PSS film under changing RH. The correlations are represented on a color bar from −1 to +1 in the lower right corner. Feature symbols are defined in Table 1. b) Errors in prediction of optical (top panel), electrical (center panel), and gravimetric/viscoelastic (bottom panel) film properties using LASSO regression when training data consist of features from a single functional mode (colored) and all measured modes (black). c) Top panel: average prediction error when the percentage of samples used for training the model is varied. Error associated with using optical data to predict optical data (O to O) is compared to error resulting from using all measured data to predict optical data (All to O), and similarly for electrical (E) and gravimetric/viscoelastic (G/V) features.

(green = gravimetric/viscoelastic, blue = electrical, red = optical), where blue correlations correspond to strong negative linear correlation, red to strong positive linear correlation, and white to no linear correlation. Features generally exhibited strong correlations with other functional modes and with RH, which suggests that many of the measured film properties can be predicted by regression.

A least absolute shrinkage and selection operator (LASSO) linear regression was used to predict gravimetric/viscoelastic ($\Delta\mu - 1$), electrical (IDC), and optical (ΔI) responses to humidity. These features were chosen as prediction targets because of their nonlinearity, strong RH response, and high correlation with other features. LASSO regression was used as a predictive model because it eliminates insignificant regression coefficients to improve interpretability of the regression, enabling simple comparison between the importance of each feature in the model. Regression results and coefficients of the LASSO model are shown in Figure S4, Supporting Information. To utilize benefits of multimodal characterization, we plotted prediction accuracy of the regression when a single functional mode was used for training data and compared it with accuracy when all measured functional modes were used for training data (Figure 5b). In all cases, supplementing training data with data from other measured modes significantly improved accuracy of the model prediction. The result sheds light on the benefits of supplementing measured data with other auxiliary features for improving predictive modeling.

It is worth noting that the absolute accuracy of any regression depends strongly on the proportion of measured data that is used for training compared to that used for testing. This effect was explored by varying the percentage of measured samples used for training and those used for testing the model (Figure 5c). When 2% of the samples are used for training, the training set consists of only four samples: features measured at 2%, 32%, 62%, and 92% RH. When 50% of the samples are used for training, the training set consists of one training sample for each integer RH value and one testing sample for each half-integer RH value. As the percentage of samples used for training increases from 2% to 50%, error of the predictive model decreases as expected (Figure 5c top panel). In all cases, errors are lower when a single functional mode is supplemented with additional functional modes. For example, when all modes are used to predict an optical mode ("All to O" in plot legend), error is significantly lower than when only optical modes are used to predict optical modes ("O to O" in legend). The enhancement in predictive accuracy is shown in the bottom panel of Figure 5c. Supplementing electrical and optical training sets with auxiliary modes resulted in ≈3.5–5% increase in prediction accuracy, while supplementing gravimetric/viscoelastic training resulted in ≈1% accuracy improvement. The effect of supplementing training sets with additional functional modes is highest when the training samples are sparse (<5% of samples used for training). The results demonstrate that low-accuracy models that rely on sparse training sets may be strongly improved by incorporation of data from other functional modes.

4. Conclusions

We developed a lab-on-a-crystal, materials science analog to "lab-on-a-chip", in which multiple functional modes of a thin film may be probed simultaneously. The lab-on-a-crystal platform is based on a QCM as a substrate for the measurements of gravimetric, viscoelastic, electrical, and optical properties under controlled environment on macro and nano scales. Top access to the film surface allows for optical probing and SFM, while auxiliary electrodes may be used for electrical characterization. We demonstrated viability of the lab-on-a-crystal platform for measuring functional properties of hydroscopic polymer PEDOT:PSS under changing environment. The effect of supplementing training sets using additional functional modes is highest when the training samples are sparse (<5% of samples used for training). The results demonstrate that low-accuracy models that rely on sparse training sets may be significantly improved by incorporation of data from other functional modes. We found correlations between PL, topography, and elastic modulus by local probing PEDOT aggregates. Significant changes in viscoelastic properties and electrical conductivity occurred in response to changes in humidity. The lab-on-a-crystal can be coupled to machine learning algorithms to understand correlations between different functionalities and shows promise for artificial controlled-controlled high-throughput materials characterization.

Supporting Information

Supporting Information is available from the Wiley Online Library or from the author.

Acknowledgements

This research was conducted at the Center for Nanophase Materials Sciences, which is a DOE Office of Science User Facility. The authors thank Melchor Varela for assistance using the SARK-110 antenna analyzer and SARK Plots software. This manuscript has been authored by UT-Battelle, LLC under contract no. DE-AC05-00OR22725 with the United States Department of Energy. The United States Government retains and the publisher, by accepting the article for publication, acknowledges that the United States Government retains a non-exclusive, paid-up, irrevocable, world-wide license to publish or reproduce the published form of this manuscript, or allow others to do so, for United States Government purposes. The Department of Energy will provide public access to these results of federally sponsored research in accordance with the DOE Public Access Plan (http://energy.gov/downloads/doe-public-access-plan).

Conflict of Interest

The authors declare no conflict of interest.

Keywords

gravimetric, impedance, machine learning, multifunctional materials, PEDOT:PSS, QCM, viscoelastic

Received: September 27, 2019
Revised: November 15, 2019
Published online:

[1] a) J. N. Cawse, *Experimental Design for Combinatorial and High Throughput Materials Development*, Wiley, New York **2003**; b) G. Kotzar, M. Freas, P. Abel, A. Fleischman, S. Roy, C. Zorman, J. M. Moran, J. Melzak, *Biomaterials* **2002**, *23*, 2737.

[2] a) M. L. Green, C. Choi, J. Hattrick-Simpers, A. Joshi, I. Takeuchi, S. Barron, E. Campo, T. Chiang, S. Empedocles, J. Gregoire, *Appl. Phys. Rev.* **2017**, *4*, 011105; b) P. Nikolaev, D. Hooper, F. Webber, R. Rao, K. Decker, M. Krein, J. Poleski, R. Barto, B. Maruyama, *npj Comput. Mater.* **2016**, *2*, 16031; c) D. P. Tabor, L. M. Roch, S. K. Saikin, C. Kreisbeck, D. Sheberla, J. H. Montoya, S. Dwaraknath, M. Aykol, C. Ortiz, H. Tribukait, *Nat. Rev. Mater.* **2018**; d) G. J. Mulholland, S. P. Paradiso, *APL Mater.* **2016**, *4*, 053207.

[3] a) R. Daw, J. Finkelstein, *Nature* **2006**, *442*, 367; b) V. Srinivasan, V. K. Pamula, R. B. Fair, *Lab Chip* **2004**, *4*, 310; c) M. L. Shuler, *Lab Chip* **2017**, *17*, 2345; d) D. R. Reyes, D. Iossifidis, P.-A. Auroux, A. Manz, *Anal. Chem.* **2002**, *74*, 2623; e) P.-A. Auroux, D. Iossifidis, D. R. Reyes, A. Manz, *Anal. Chem.* **2002**, *74*, 2637.

[4] a) N. Balar, Y. Xiong, L. Ye, S. Li, D. Nevola, D. B. Dougherty, J. Hou, H. Ade, B. T. O'Connor, *ACS Appl. Mater. Interfaces* **2017**, *9*, 43886; b) B. O'Connor, E. P. Chan, C. Chan, B. R. Conrad, L. J. Richter, R. J. Kline, M. Heeney, I. McCulloch, C. L. Soles, D. M. DeLongchamp, *ACS Nano* **2010**, *4*, 7538.

[5] a) M. Gerosa, A. Sacco, A. Scalia, F. Bella, A. Chiodoni, M. Quaglio, E. Tresso, S. Bianco, *IEEE J. Photovoltaics* **2016**, *6*, 498; b) A. M. Gaikwad, A. C. Arias, D. A. Steingart, *J. Energy Technol.* **2015**, *3*, 305; c) Z. Chai, J. Gu, J. Khan, Y. Yuan, L. Du, X. Yu, M. Wu, W. Mai, *RSC Adv.* **2015**, *5*, 88052; d) A. E. Ostfeld, A. M. Gaikwad, Y. Khan, A. C. Arias, *Sci. Rep.* **2016**, *6*, 26122.

[6] a) T. Wang, Y. Guo, P. Wan, H. Zhang, X. Chen, X. Sun, *Small* **2016**, *12*, 3748; b) C. Wu, T. W. Kim, F. Li, T. Guo, *ACS Nano* **2016**, *10*, 6449; c) J. Kim, J. R. Sempionatto, S. Imani, M. C. Hartel, A. Barfidokht, G. Tang, A. S. Campbell, P. P. Mercier, J. J. A. S. Wang, *Adv. Sci.* **2018**, *5*, 1800880; d) J. Liang, K. Tong, Q. Pei, *Adv. Mater.* **2016**, *28*, 5986.

[7] a) C. R. Oliver, W. Westrick, J. Koehler, A. Brieland-Shoultz, I. Anagnostopoulos-Politis, T. Cruz-Gonzalez, A. J. Hart, *Rev. Sci. Instrum.* **2013**, *84*, 3565; b) T. F. Jaramillo, S.-H. Baeck, A. Kleiman-Shwarsctein, K.-S. Choi, G. D. Stucky, E. W. McFarland, *J. Comb. Chem.* **2005**, *7*, 264; c) J. C. Meredith, A. P. Smith, A. Karim, E. J. Amis, *Macromolecules* **2000**, *33*, 9747; d) T. Iwasaki, N. Itagaki, T. Den, H. Kumomi, K. Nomura, T. Kamiya, H. Hosono, *Appl. Phys. Lett.* **2007**, *90*, 242114.

[8] a) H. D. Espinosa, Y. Zhu, N. Moldovan, *J. Microelectromech. Syst.* **2007**, *16*, 1219; b) S. Zhang, M. U. Ocheje, S. Luo, D. Ehlenberg, B. Appleby, D. Weller, D. Zhou, S. Rondeau-Gagné, X. Gu, *Macromol. Rapid Commun.* **2018**, *39*, 1800092; c) N. S. Güldal, T. Kassar, M. Berlinghof, T. Ameri, A. Osvet, R. Pacios, G. L. Destri, T. Unruh, C. J. Brabec, *J. Mater. Chem. C* **2016**, *4*, 2178; d) X. Gu, I. Gunkel, A. Hexemer, W. Gu, T. P. Russell, *Adv. Mater.* **2014**, *26*, 273; e) A. Yadav, A. Lokhande, R. Pujari, J. Kim, C. Lokhande, *J. Colloid Interface Sci.* **2016**, *484*, 51; f) J. S. Lee, K.-Y. Shin, O. J. Cheong, J. H. Kim, J. Jang, *Sci. Rep.* **2015**, *5*, 7887; g) N. Kumar, B. K. Gupta, A. Srivastava, H. Patel, P. Kumar, I. Banerjee, T. N. Narayanan, G. Varma, *Sci. Adv. Mater.* **2015**, *7*, 1125; h) C. Hao, Y. Liu, X. Chen, J. Li, M. Zhang, Y. Zhao, Z. Wang, *Small* **2016**, *12*, 1825.

[9] a) G. Sauerbrey, *Z. Phys.* **1959**, *155*, 206; b) M. Voinova, M. Jonson, B. Kasemo, *Biosens. Bioelectron.* **2002**, *17*, 835.

[10] a) M. V. Voinova, M. Rodahl, M. Jonson, B. Kasemo, *Phys. Scr.* **1999**, *59*, 391; b) K. K. Kanazawa, J. G. Gordon, *Anal. Chem.* **1985**, *57*, 1770.

[11] a) M. Tatarko, E. S. Muckley, V. Subjakova, M. Goswami, B. G. Sumpter, T. Hianik, I. N. Ivanov, *Sens. Actuators, B* **2018**, *272*, 282; b) I. Koshets, Z. Kazantseva, Y. M. Shirshov, S. Cherenok, V. Kalchenko, *Sens. Actuators, B* **2005**, *106*, 177; c) M. Rodahl, F. Höök, A. Krozer, P. Brzezinski, B. Kasemo, *Rev. Sci. Instrum.* **1995**, *66*, 3924; d) L. Rodriguez-Pardo, J. Fariña, C. Gabrielli, H. Perrot, R. Brendel, *Sens. Actuators, B* **2004**, *103*, 318.

[12] a) E. S. Muckley, C. B. Jacobs, K. Vidal, N. V. Lavrik, B. G. Sumpter, I. N. Ivanov, *Sci. Rep.* **2017**, *7*, 9921; b) E. S. Muckley, C. B. Jacobs, K. Vidal, J. P. Mahalik, R. Kumar, B. G. Sumpter, I. N. Ivanov, *ACS Appl. Mater. Interfaces* **2017**, *9*, 15880; c) E. S. Muckley, N. Miller, C. B. Jacobs, T. Gredig, I. N. Ivanov, *J. Photonics Energy* **2016**, *6*, 045501; d) C. B. Jacobs, A. V. Ievlev, L. F. Collins, E. S. Muckley, P. C. Joshi, I. N. Ivanov, presented at SPIE Organic Photonics + Electronics San Diego, CA, August–September **2016**; e) E. Muckley, M. Naguib, I. N. Ivanov, *Nanoscale* **2018**; f) E. S. Muckley, L. F. Collins, A. V. Ievlev, X. Ye, K. Kisslinger, B. G. Sumpter, N. V. Lavrik, C.-Y. Nam, I. N. Ivanov, *ACS Appl. Mater. Interfaces* **2018**; g) E. S. Muckley, M. Naguib, H.-W. Wang, L. Vlcek, N. C. Osti, R. L. Sacci, X. Sang, R. R. Unocic, Y. Xie, M. Tyagi, *ACS Nano* **2017**, *11*, 11118.

[13] U. Lang, N. Naujoks, J. Dual, *Synth. Met.* **2009**, *159*, 473.

[14] a) E. S. Muckley, J. Lynch, R. Kumar, B. Sumpter, I. N. Ivanov, *Sens. Actuators, B* **2016**; b) E. S. Muckley, C. Anazagasty, C. B. Jacobs, T. Hianik, I. N. Ivanov, presented at SPIE Organic Photonics + Electronics, San Diego, CA, August–September **2016**.

[15] M. Kocun, A. Labuda, W. Meinhold, I. Revenko, R. Proksch, *ACS Nano* **2017**, *11*, 10097.

[16] a) A. M. Nardes, R. A. Janssen, M. Kemerink, *Adv. Funct. Mater.* **2008**, *18*, 865; b) M. Döbbelin, R. Marcilla, M. Salsamendi, C. Pozo-Gonzalo, P. M. Carrasco, J. A. Pomposo, D. Mecerreyes, *Chem. Mater.* **2007**, *19*, 2147.

[17] a) A. M. Nardes, M. Kemerink, R. A. Janssen, J. A. Bastiaansen, N. M. Kiggen, B. M. Langeveld, A. J. van Breemen, M. M. de Kok, *Adv. Mater.* **2007**, *19*, 1196; b) S. Timpanaro, M. Kemerink, F. Touwslager, M. De Kok, S. Schrader, *Chem. Phys. Lett.* **2004**, *394*, 339.

[18] a) J. Qu, L. Ouyang, C.-C. Kuo, D. C. Martin, *Acta Biomater.* **2016**, *31*, 114; b) A. J. Nolte, M. F. Rubner, R. E. Cohen, *Macromolecules* **2005**, *38*, 5367; c) F. Greco, A. Zucca, S. Taccola, A. Menciassi, T. Fujie, H. Haniuda, S. Takeoka, P. Dario, V. Mattoli, *J. Soft Matter* **2011**, *7*, 10642.

[19] B. W. Neubig, in *Proc. of IEEE 48th Annual Symp. on Frequency Control*, IEEE, Piscataway, NJ **1994**, pp. 268–272.

[20] a) L. Bruschi, A. Carlin, G. Mistura, *Phys. Rev. Lett.* **2002**, *88*, 046105; b) J. Krim, D. Solina, R. Chiarello, *Phys. Rev. Lett.* **1991**, *66*, 181; c) K. M. Persson, R. Gabrielsson, A. Sawatdee, D. Nilsson, P. Konradsson, M. Berggren, *Langmuir* **2014**, *30*, 6257.

[21] a) N. C. Speller, N. Siraj, B. P. Regmi, H. Marzoughi, C. Neal, I. M. Warner, *Anal. Chem.* **2015**, *87*, 5156; b) V. M. Mecea, *Anal. Lett.* **2005**, *38*, 753.

[22] a) A. Lenz, H. Kariis, A. Pohl, P. Persson, L. Ojamäe, *Chem. Phys.* **2011**, *384*, 44; b) K. L. Mulfort, J. Ryu, Q. Zhou, *Polymer* **2003**, *44*, 3185.

[23] Y. Xia, J. Ouyang, *J. Mater. Chem.* **2011**, *21*, 4927.

[24] M. Kuş, S. Okur, *Sens. Actuators, B* **2009**, *143*, 177.

[25] M. M. de Kok, M. Buechel, S. Vulto, P. van de Weijer, E. Meulenkamp, S. de Winter, A. Mank, H. Vorstenbosch, C. Weijtens, V. van Elsbergen, *Phys. Status Solidi A* **2004**, *201*, 1342.

[26] B. Sarkar, M. Jaiswal, D. K. Satapathy, *J. Phys.: Condens. Matter* **2018**, *30*, 225101.

[27] Y.-Y. Lee, G. M. Choi, S.-M. Lim, J.-Y. Cho, I.-S. Choi, K. T. Nam, Y.-C. Joo, *Sci. Rep.* **2016**, *6*, 25332.

[28] T. Kinkeldei, C. Zysset, K. Cherenack, G. Tröster, in *2011 16th Int. Solid-State Sensors, Actuators and Microsystems Conf.*, IEEE, Piscataway, NJ **2011**, pp. 1156–1159.

